Superhydrophobic Fluorinated Carbon Powders for Improved Water Management in Hydrogen Fuel Cells

E. M. CAN[1], A. Mufundirwa[2], P. Wang[3], S. Iwasaki[3], T. Kitahara[3,4], H. Nakajima[3,4,5], M. Nishihara[5], K. Sasaki [3,4,5,6,7], S. M. Lyth[1,6,7,8*]

[1]Department of Automotive Science, Graduate School of Integrated Frontier Sciences, Kyushu University, 744 Motooka, Nishi-ku, Fukuoka, 819-0395 Japan

[2]Japan Synchrotron Radiation Research Institute (JASRI)/SPRING-8, Sayo, Hyogo 679-5198, Japan

[3]Department of Hydrogen Energy Systems, Graduate School of Engineering, Kyushu University, 744 Motooka, Nishi-ku, Fukuoka 819-0395, Japan

[4]Department of Mechanical Engineering, Faculty of Engineering, Kyushu University, 744 Motooka, Nishi-ku, Fukuoka 819-0395, Japan

[5]Next-Generation Fuel Cell Research Center (NEXT-FC), Kyushu University, 744 Motooka, Nishi-ku, Fukuoka 819-0395, Japan

[6]International Research Center for Hydrogen Energy, Kyushu University, 744 Motooka, Nishi-ku, Fukuoka, 81970395 Japan

[7]International Institute for Carbon-Neutral Energy Research, Kyushu University, 744 Motooka, Nishi-ku, Fukuoka, 819-0395 Japan

[8]Department of Mechanical Engineering, Faculty of Engineering, University of Sheffield, Ella Armitage Building, Sheffield, S3 7RD, United Kingdom

Abstract

Under high current density operation, the efficiency of polymer electrolyte fuel cells (PEFCs) can dramatically decrease. This is due to water accumulation at the cathode side, preventing oxygen diffusion to the electrocatalyst. As such, effective water management is of vital importance by use of a suitable gas diffusion layer (GDL) and/or microporous layer (MPL). MPLs generally consist of carbon black as the porous electron conducting phase, and polytetrafluoroethylene (PTFE) as a hydrophobic binder. Here, we instead use superhydrophobic fluorinated carbon powder in the MPL as a novel material to decrease the required PTFE content. It is confirmed that the water contact angle of the MPL can be increased from 131° to 151° by using fluorinated carbon. Moreover, the fluorinated carbon MPL shows lower oxygen transport resistance at high humidity. Furthermore, in single fuel cell tests at various temperatures and relative humidity values, the I-V performance is significantly and consistently better than for the conventional MPL. These results confirm that fluorinated carbon is a promising new material for water management in the MPLs of PEFCs.

Keywords: Microporous layers; carbon nanomaterials; electrochemistry; water contact angle; fluorinated carbon, PEFCs

1. Introduction

Global heating, worsening air quality, and energy security issues mean that governments across the globe are striving to find alternatives to fossil fuels [1–3]. Renewable energy technologies such as wind and solar power are in the process of revolutionizing the energy industry, but issues such as intermittency and long-term energy storage are hampering decarbonization efforts. Hydrogen could be the key to solving these issues, providing a versatile energy storage medium and fuel, with polymer electrolyte fuel cells (PEFCs) enabling direct conversion of hydrogen to electricity. PEFCs are electrochemical energy conversion devices where hydrogen and oxygen react to efficiently generate a voltage, and can operate with high power density [4]. Recently, PEFCs have been commercialized in fuel cell electric vehicles (FCEVs) such as the Toyota MIRAI in Japan. However, for global scale up of PEFC systems, a significant reduction in cost is necessary. This can be achieved in three ways: (i) reducing the component cost; (ii) improving system durability; or (iii) increasing system efficiency [5–8].

In PEFCs, the gas diffusion layer (GDL) is located between the catalyst layer and the flow channel. This component is primarily made of carbon fiber, and has several roles including: (i) the supply of reactant gases; (ii) the exhaust of products; (iii) electrical connectivity; and (iv) water management [9]. At the cathode side of the membrane electrode assembly (MEA), oxygen is supplied through the GDL to the catalyst layer, where water is formed via the oxygen reduction reaction (ORR). The water generated in the catalyst layer is then ideally transported back through the GDL to the flow channel, eventually leaving the system via the exhaust. However, in circumstances where high power output is required, the rate of water generation

in the catalyst layer increases. This can lead to water accumulation, preventing oxygen diffusion to the platinum catalyst surface, and causing a significant voltage drop. This phenomenon is called ‘flooding’, and decreases PEFC efficiency under high current density conditions [10].

To minimize flooding and improve water management, the carbon fibers in GDLs are generally coated with a thin layer of polytetrafluoroethylene (PTFE) to render them hydrophobic. In addition, a microporous layer (MPL) is used at the interface with the catalyst layer to aid water transport [11–15]. The MPL usually consists of carbon black with a hydrophobic binder such as PTFE. In the absence of an MPL, GDLs is prone to severe flooding under high current density operation [15–17]. Therefore, the choice of an MPL with suitable properties is critical for water management in PEFCs.

There have been numerous studies on MPLs investigating the type of material used, the pore structure, the thickness, the PTFE content, and different wettability designs [1,10,11,13–26]. The PTFE content in the MPL is reported to significantly affect PEFC performance, with lower PTFE content leading to a greater likelihood of flooding. Higher PTFE content is reported to reduce the pore size, leading to lower gas permeability and thus higher diffusion losses. In addition, PTFE is electronically insulating, so higher PTFE loadings can lead to increased ohmic losses [29]. As such alternatives solutions to water management in PEFCs in which the amount of PTFE used is reduced could be highly advantageous.

Fluorination is an effective method for enhancing the hydrophobic properties of carbon materials [30–32]. Fluorination of carbon can be achieved directly via heat treatment in the presence of pressurized fluorine gas. Indirect fluorination involves thermal decomposition of a fluorine source such as xenon difluoride (XeF_2) generating fluorine radicals which react with the carbon surface. Alternatively,

surface functionalization can be achieved via plasma treatment in CF_4. Direct fluorination and indirect fluorination both involve toxic gases or solvents. In addition, direct fluorination is highly exothermic, and great care must be taken over safety. Furthermore, plasma treatment can only functionalize the surface of carbon exposed to the plasma, making it difficult to apply this method to bulk carbon materials. Various related materials have been reported, including fluorinated carbon nanotubes [33–35], fluorinated carbon fibers [36–38], fluorinated graphene [39–42], and fluorinated carbon black [30,43–45]. These have been used in applications such as water-repellent sprays [46], gas sensors [47], lubricants, and lithium-ion batteries [48,49].

Fluorinated carbon materials have also been explored in PEFCs in several reports. For example, Nguyen et al. investigated fluorination of carbon fibers in the GDL via direct fluorination in fluorine gas and reported improved I-V performance in the mass diffusion limited current density region [13]. Carbon monofluoride decorated with platinum has been reported to be an effective electrocatalyst with high mass activity in PEFCs and enhanced mass diffusion in direct methanol fuel cells (DMFCs) [50]. Similarly, fluorinated carbon decorated with platinum as a cathode catalyst has been reported to improve durability by suppressing carbon corrosion. [51,52]. However, to the best of our knowledge there are no reports on the utilization of fluorinated carbons in the MPL of PEFCS.

In previous work, our group synthesized superhydrophobic fluorinated carbon nanoparticles at gram scale, using a unique solvothermal synthesis technique [27]. Here, this class of fluorinated carbon is employed as an alternative material for the MPL in PEFCs, as an attempt to improve water management and PEFC performance at high current density.

2. Experimental

2.1 Synthesis and Characterization of Fluorinated Carbon

2 g of sodium lumps (Sigma-Aldrich, Japan) and 5 ml (8.25g) of tridecafluorooctan-1-ol (Funakoshi Co, Ltd) were added to a 100 ml PTFE-lined pressure vessel (Flon Industry) which was sealed in a stainless-steel protective jacket. The reaction vessel was then placed in an oven at 150 °C for 24 hours before being cooled completely and carefully opened. After the reaction, the product was collected and sonicated in a mixture of 50 vol.% deionized water and 50 vol.% ethanol for 30 minutes, then stirred for 24 hours to remove byproducts. After this, the product was vacuum filtered using an Omnipore ™ 0.2 μm membrane filter. Finally, the product was dried for 24 hours in an oven at 65°C. The final mass of product obtained was 1.53 g, corresponding to a yield of 18.5 % (relative to the tridecafluorooctan-1-ol precursor).

The product was characterized by X-ray photoelectron spectroscopy (XPS, PHI 5000 Versa probe (II) ULVAC); transmission electron microscopy (JEM-2100HC); scanning electron microscopy and energy dispersive X-ray analysis (FE-SEM, JSM-7900F); nitrogen adsorption analysis (Belsorp Mini X, Microtrac MRB) and water contact angle measurement (DMs-401, Kyowa Interface Science Co., Ltd, Japan). Furthermore, thermogravimetric analysis (TGA, Rigaku Thermo plus EVO2 TG8121) was conducted in air.

2.2 Preparation of the MPL

Carbon black (Sigma-Aldrich, Japan)[53] MPLs (CB-MPL) and fluorinated carbon MPLs (FC-MPL) were manufactured using identical processes. An MPL slurry was prepared by adding 2 g of carbon (either CB or FC), 0.5 g of methyl cellulose pore forming agent (Fujifilm Wako Chemicals, Japan), 14 ml of deionized water (Milli-Q, 18 MΩ cm), and 0.1 ml of Triton X-100 (Sigma-Aldrich, Japan) surfactant to a 100 ml polypropylene beaker. This mixture was homogenized for 15 min at 2000 rpm (Thinky Mixer AR-100). Then, 0.059 ml (corresponding to 0.089 g) of PTFE dispersion (60 wt%, TeflonTM 30B from Polysciences, Inc)[54] was added to the mixture as a binder, followed by a second homogenization step for 15 min at 2000 rpm. To coat the MPL onto the Toray-GDL (5 wt% wetproofed TGP-H-060 Toray Paper), a 5 cm × 5 cm square of GDL was placed on a glass plate, and a 75 μm thick stainless-steel mask with 3 cm × 3 cm opening was placed on top of the GDL. The MPL slurry was then coated onto the GDL using a doctor blade, then dried at 65 °C for one hour. Finally, the MPL-coated GDLs were heat-treated at 400°C for one hour under air, to sinter the PTFE binder and decompose the methyl cellulose pore forming agent as well as any remaining Triton-X surfactant. Decomposition of these materials is confirmed by TGA in Fig. S1.

In addition, free-standing MPLs were fabricated to aid with calculation of the porosity, by coating the slurry directly on a glass plate instead of a GDL, followed by the same drying and sintering steps. Several studies have reported an optimized PTFE loading in MPLs of about 20% [29,55,56]. One purpose of this study is to minimize the PTFE loading. Through trial-and-error, we determined that ~5 wt% PTFE loading was the minimum limit required to create mechanically stable free-standing MPLs. Thus, all the MPLs investigated here have a thickness of ~35 μm and 5 wt% PTFE content. The MPL porosities were calculated from the thickness,

area, mass, and density of the different components using the following equation [57]:

$$\emptyset = 1 - \frac{V_S}{V_{MPL}} = 1 - \frac{m_{MPL} \cdot (\omega_c/\rho_c + \omega_B/\rho_B)}{d_{MPL} \cdot A} \qquad [1]$$

where $\emptyset$ is the porosity of the MPL; V_S is the volume of the solid components (i.e. either PTFE and CB or PTFE and superhydrophobic fluorinated carbon (SHFC)); V_{MPL} is the geometric volume of the MPL; m_{MPL} is the mass of the MPL; ω_c is the mass fraction of the carbon component (0.95); ω_B is the mass fraction of the PTFE binder (0.05); ρ_c is the density of the carbon component; ρ_B is the density of the PTFE binder; d_{MPL} is the thickness of the MPL; and A is the area of the MPL (1 cm $\times$ 1 cm).

2.3 Preparation of the Membrane Electrode Assembly (MEA)

The catalyst ink was prepared by mixing Pt/C (TEC10E50E, lot 1019-8581, 46.8 wt_{Pt}%, Tanaka, Japan) with 5 wt% Nafion solution (Wako, Japan), deionized water, and super-dehydrated ethanol (99.5 vol%, Wako, Japan). The catalyst ink was stirred overnight, then sonicated for 30 minutes just before use (SMT Corporation, Ultra Sonic Homogenizer UH-600). Nafion 212 membranes were placed onto movable-hot plate and masked, leaving an exposed area of 1 cm^2. The catalyst ink was then sprayed directly onto the Nafion membrane using pulsed spray mode from an automated spraying device (Nordson K.K., C3J), with a catalyst loading of 0.3 mg_{Pt}/cm^2 and a Nafion content of 28 wt% [58], at both the anode and cathode. The

resulting MEAs were finally hot pressed at 132 °C and 0.3 kN for 180 s (Sinto Digital Press CYPT-10).

2.4 Thermogravimetric Analysis Tests

During preparation the MPL, a slurry was prepared with methyl cellulose and Triton-X to improve the dispersibility and rheological properties for printing onto the GDL. These are assumed to decompose during heat treatment of the resulting MPL-coated GDL at 400°C. To confirm this, TGA was conducted on methyl cellulose and Triton-X under similar heat treatment conditions (Fig. S1).

2.5 Fuel Cell Polarization Tests

Fuel cell tests were performed using a 1 cm^2 active area single cell obtained from the Japanese Automotive Research Institute (JARI) with serpentine type flow fields. The performance of the different MPL-coated GDLs was investigated by measuring polarization curves at two different cell temperatures (45 °C and 80 °C). The temperature of 80ºC was selected to reproduce conventional PEFCs operating conditions. The lower temperature of 45 ºC was selected as an extreme condition in which water condensation readily causes flooding even at lower current density, to highlight the effect of using superhydrophobic MPLs. Three different conditions of relative humidity (RH) were also tested (80 %, 100 %, 120 %) at both the anode and cathode. To reach 120% relative humidity with a cell temperature of 80 °C, the humidifier temperature was maintained at 85 °C. For a cell temperature of 45 °C, the humidifier was held at 49 °C. Fuel cell performance tests at 120% RH and 80 °C are not shown because of water condensation in uninsulated sections of the pipes

between the cell and the humidifier (85 ºC), disrupting the gas flow and preventing stable cell I-V performance from being measured.

The constant volumetric flow rates were 0.139 L/min hydrogen and 0.332 L/min oxygen at anode and cathode, respectively (counter flow conditions). A fuel cell test station (AUTOPEM-CVZ01, Toyo Corporation, Japan) was used to control the humidification, cell temperature, and gas flow. Polarization curves were measured using an electrochemical interface impedance analyzer (Solartron SI-1287). Prior to the polarization curve measurement, each cell was conditioned at 0.6 V for 5 hours.

2.6 Air Permeability Tests

Through-plane (transverse) air permeability tests were conducted under ambient conditions with dry air flow, using the set up summarized in Ref [59], applying Darcy's law (Eq.2): [60]

$$Q = \frac{\mathrm{K} \cdot A \cdot \Delta P}{\mu \cdot L} \qquad [2]$$

where Q is the volumetric flow rate (m^3s^{-1}); K is the air permeability (m^2); A is the area of GDL or MPL coated GDL (0.5 cm^2); ΔP is the pressure difference between the inlet and outlet; μ is Newtonian viscosity (18.37 $kgm^{-1}s$); and L is the sample thickness (m). To measure air permeability, a 1 cm × 1 cm GDL sample was placed between two plates, each with a 0.5 cm^2 diameter hole for air flow. To avoid leakage, PTFE gaskets were also used. The compression was set to 1 MPa, similar to the pressure used in PEFC polarization measurements. The air pressure was set by the volumetric flow rate to by 1.23 kPa, as suggested in the Gurley Method [61].

2.7 Water Contact Angle Measurements

The water contact angles (WCAs) of the different MPLs were measured in two different ways. In the first method, the surface contact angle was measured using the pendant drop method with an automated analyzer (DMs-401, Kyowa Interface Science Co., Ltd, Japan). All GDLs have a PTFE loading of 5 wt%. Contact angles were measured using the pendant drop method. To minimize the effect of gravity, the droplet size was fixed at around 1 μL. To measure the contact angle of the as-synthesized fluorinated carbon powder, it was first pressed between two glass plates to create a relatively smooth surface.

In the second method, the internal contact angle of the pores was measured using the set up summarized in Ref [59], and by applying the Young-Laplace equation (Eq.3):

$$\mathrm{d} = \frac{4 \cdot \sigma \cdot \cos\theta}{P_C} \qquad [3]$$

where d is the pore diameter; σ is the surface tension of the liquid; θ is the contact angle, and P_C is the capillary pressure. To measure the contact angle within the largest pore, first the maximum pore size of the MPL was calculated using Eq.3. To measure the maximum pore size, samples were immersed in a low surface tension liquid (Galpore, σ = 0.0156 Nm^{-1}, contact angle = 0 º) in a vacuum desiccator for two hours. Then, the MPL sample was carefully removed, placed in the sample holder, and sealed with a PTFE gasket. Then, air flow was supplied through the plane of the sample, and the inlet air pressure recorded. Since the largest pore has the lowest capillary pressure, it can be assumed that this will be the first to be blown

out. The pressure at which this first occurs is then used in Eq.3. to estimate the maximum pore diameter [60]. After this maximum pore size calculation, pressurized water was then supplied to the same sample. The pressure at which water starts to flow though the largest pore of the GDL corresponds to the water breakthrough pressure. After determination of water breakthrough pressure, the contact angle of the pores can be calculated via Eq.3. Here, the surface tension of water at 25° C is assumed to be 0.0720 Nm^{-1}, and samples size was 0.5 cm^2.

2.8 Oxygen Transport Resistance

The total oxygen transport resistance was calculated from the limiting current density under the differential relative humidity conditions of the supplied gasses, using the following equation [62]:

$$R_T = \frac{4 \cdot F \cdot P_{O_2}}{i_{lim} \cdot R \cdot T} \qquad [4]$$

Where R_T is the total oxygen transport resistance of the cell (sm^{-1}), F is the Faraday constant (96485 C mol^{-1}), P_{O_2} is the oxygen partial pressure (Pa), R is the gas constant (8314 J $mol^{-1}K^{-1}$), T is the cell temperature (K) and i_{lim} is the limiting current density at 0.2 V.

The oxygen transport resistance was calculated at both 80 °C and 45 °C cell temperature conditions for each different MPL. At high cell temperature, the oxygen transport resistance was measured at relative humidity of 80, 100, and 120 %. At low cell temperature, the oxygen transport resistance was measured at 80, 100, 120, 160, and 200 % relative humidity. The flow rate of the supplied gases at both the

anode and cathode was 1 L/min. The oxygen concentration was 2 vol% at the cathode side, and nitrogen was used as the balance gas.

3. Results and Discussion

3.1 Material Characterization

The synthesized product was a dry black powder (fluorinated carbon) mixed with a white residue, confirmed by XPS to be sodium fluoride. This NaF was almost completely removed during the washing step. When added to water, the final product was clearly highly hydrophobic, floating readily on the surface. The microstructure of the powder was investigated by SEM and TEM (Fig. 1), revealing a spheroidal microstructure similar to carbon black (Fig.S3) [17]. The nanoparticles are clustered together with a flocculent structure, leaving micron-scale voids. The TEM images show that the particles are spheroidal and solid, with most particle sizes varying between around 50 and 100 nm in diameter. These SEM and TEM images are representative, although several much larger particles around 500 nm in diameter were also observed in some images (Fig. S2).

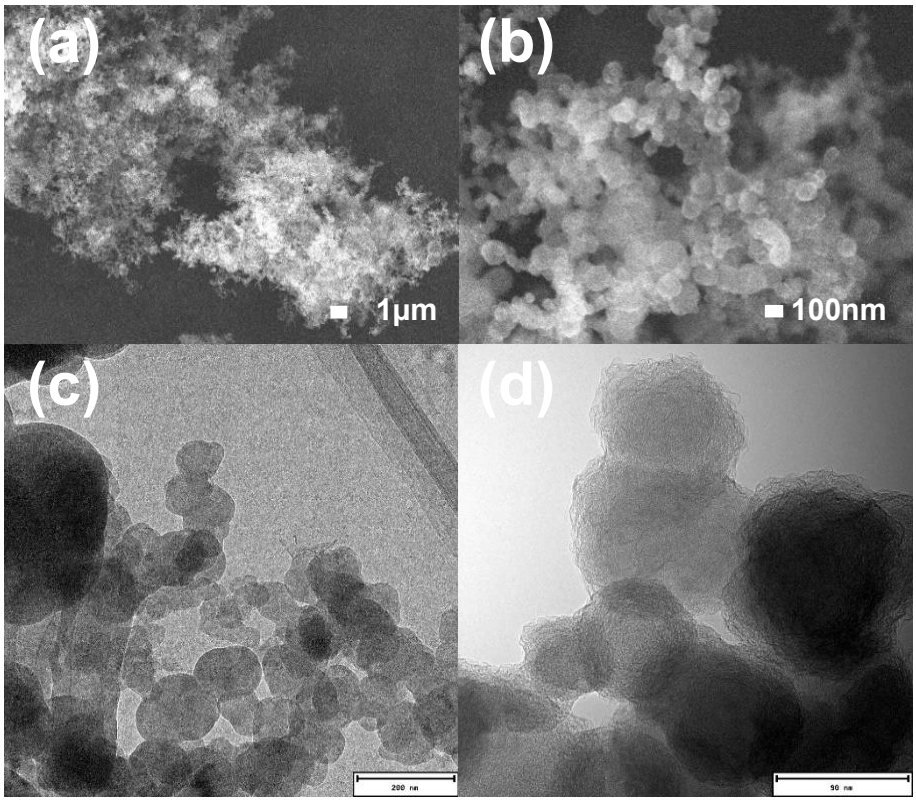

Figure 1: Electron microscopy showing the microstructure of the fluorinated carbons used in this study: (a-b) SEM images, (c-d) TEM images.

EDX reveals a carbon content of 91.6 at.%, an oxygen content of 6.3 at.%, a fluorine content of 1.9 at.%, and a sodium content of 0.2 at.%. These results confirm that this synthesis method can be used to successfully generate fluorinated carbon with relatively high fluorine content. Fig. 2 shows representative elemental EDX mapping of the fluorinated carbon powder. The presence of fluorine is confirmed throughout the whole structure, indicating that it is uniformly bonded to the carbon atoms. Meanwhile, in some areas, fluorine and sodium signals have overlapping and high intensity signals, indicating the presence of sodium fluoride. It is likely that this sodium fluoride is encapsulated within the fluorinated carbon particles, preventing it from being removed during the washing step, as observed in our previous study [30]. Increasing the length of the washing step to 3 days had no significant effect on

the sodium content. Since the sodium content is so low (0.2 at.%) and the NaF is encapsulated, its presence is not expected to have a significant impact on the initial PEFC results. However, in the case of severe carbon corrosion the effect of leaching of sodium and fluoride ions on PEFC performance should be considered. Durability will be the topic of a future study.

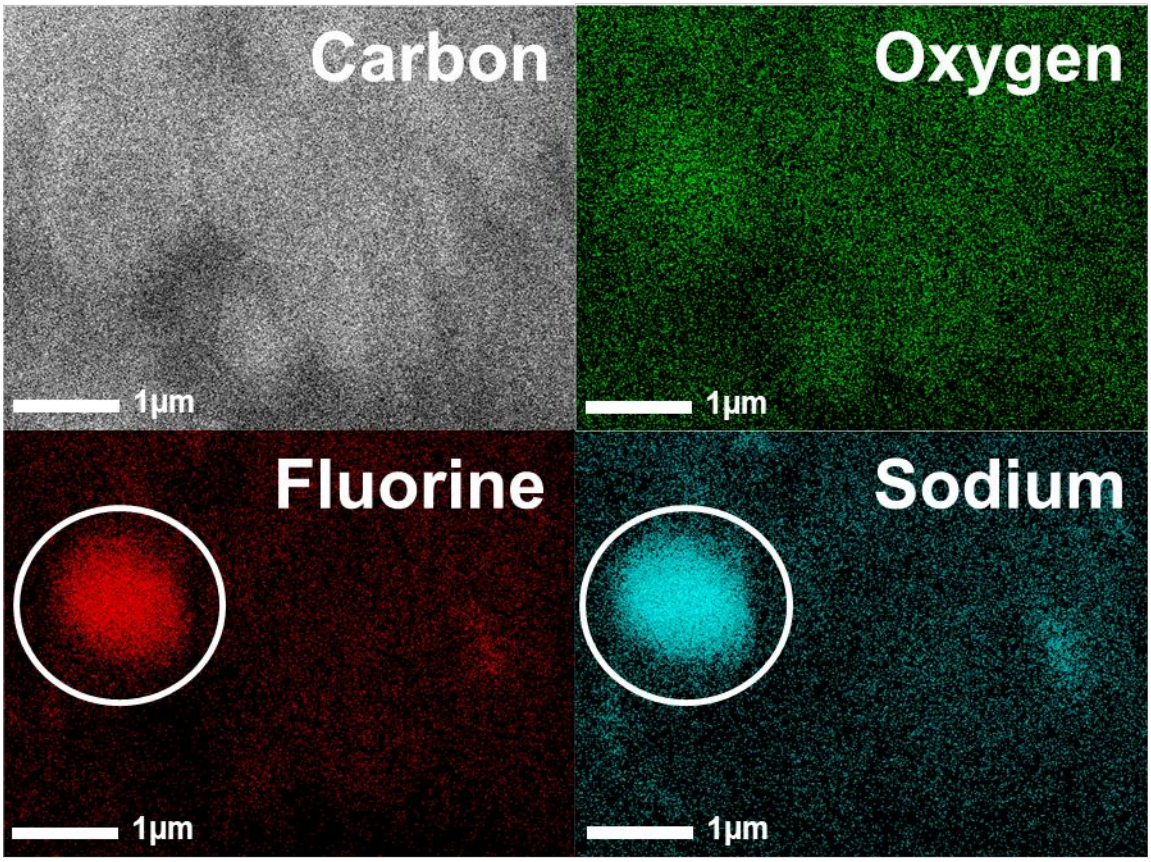

Figure 2: EDX elemental maps of fluorinated carbon.

Nitrogen adsorption/desorption isotherms of the fluorinated carbon compared with graphitized carbon black are shown in Fig. S4. Brunauer-Emmett-Teller (BET) and Barrett-Joyner-Halenda (BJH) methods were used to calculate the specific surface

area and pore size distribution. Both samples have Type Ⅲ isotherms, characteristic of nonporous materials [63]. The specific surface area of the fluorinated carbon is 40 m^2/g. This is much lower compared to non-fluorinated porous carbons prepared in a similar manner and previously reported by our group [7,45]. This is mainly attributed to the preferential formation of NaF in this case over NaOH, which acts as an activation agent in our unfluorinated carbons. Meanwhile, differences in pressure within the PTFE crucible and the viscosity of the melting precursors as they decompose may also be a factor. Furthermore, fluorination has been previously reported to decrease surface area and pore volume by blocking micropores [31]. Nevertheless, the surface area is of a similar order to that of the graphitized carbon black reference sample (115 m^2/g), suggesting that this relatively low surface area is not necessarily an issue for MPL-related applications. BJH results also confirm that the fluorinated carbon is non-porous. On the other hand, graphitized carbon black shows a certain pore size distribution between 20 and 100 nm. However, when compared with other porous carbon materials, graphitized carbon black can also effectively be considered as non-porous [6,46].

The skeletal density of the samples was measured by adding 5 ml of ethanol into a graduated cylinder, and then sample powder was added until the volume increased by exactly 0.1 ml. The increase in mass was measured and the density calculated by dividing this number by the volume displaced. Using this method, the skeletal density of graphitized carbon black was measured to be 1.9 g cm^{-3} which is within the range quoted by the manufacturer (i.e. 1.5 to 1.9 g cm^{-3}) [64]. The density of the fluorinated carbon was measured to be 2.04 g cm^{-3}. This higher density compared to carbon black is attributed to the fact that fluorine has a higher atomic mass compared to carbon.

Assuming that the carbon particles are spherical and non-porous (as discussed in the previous paragraph), the mean particle size can be calculated using the following equation [65]:

$$L_D = 6000/(\rho_s \cdot a_{s,BET}) \qquad [5]$$

where, L_D is mean particle diameter, ρ_s is the density of the adsorbent, and $a_{s,BET}$ is the BET specific surface area. According to this equation, the mean particle diameter of carbon black 27.4 nm, in close agreement with data quoted by the manufacturer (24 nm) [53], confirming that this method is reliable. Meanwhile, the mean particle size of the fluorinated carbon sample is calculated to be 74.4 nm, which is in close agreement with the particle size observed in the SEM and TEM images (Fig.1.).

XPS analysis of the fluorinated carbon (Fig. 3) confirms the presence of carbon at 284.5 eV (88.5 at.%), fluorine at 688 eV (9.8 at.%), oxygen at 532 eV (1.5 at.%), and trace amounts of sodium at 1073 eV (0.2 at.%). Two F KLL Auger peaks are also observed at 632 eV and 658 eV. The C1s narrow scan spectrum is deconvoluted into peaks corresponding to: sp^2 carbon at 284.5 eV; sp^3 carbon bond at 285.2 eV; C-O bonds at 287.5 eV; C-F bonds at 289.6 eV; CF_2 bonds at 291.5 eV; and CF_3 bonds (or C 1s shake-up) at 294.0 eV [32–36]. The F1s spectrum is deconvoluted into covalently bonded fluorine at 688.5 eV and 692.0 eV. The O1s spectrum is deconvoluted into two main peaks corresponding to C-O bonds at 532.5 eV, and possibly a sodium auger peak at 537.5 eV. Finally, the Na 1s spectrum can be fitted by a single peak at 1072.4 eV, corresponding to sodium-fluorine bonds. This analysis confirms that fluorine atoms were successfully covalently doped into the carbon structure.

The atomic concentration of fluorine obtained from XPS analysis (9.8 at.%) is significantly higher than that measured by EDX (1.9 at.%). This discrepancy is attributed to the fact that XPS is a quasi-surface sensitive analysis technique with a penetration depth of ~5-10 nm, and EDX is a bulk measurement technique with a penetration depth of 1-2 μm. The difference in measured values can be explained by the fact that the fluorination mostly occurs near the surface of the carbon, so XPS detects a high fluorine content, but EDX detects the average fluorine content throughout the whole sample, which is much lower. This may be advantageous for electronic applications. Since fluorine is a highly electronegative element, high levels of fluorine doping are expected to dramatically decrease the electronic conductivity of carbon. However, surface fluorination means that the bulk carbon retains high conductivity whilst the surface can take on the advantageous hydrophobic properties. This is especially important in the MPL in which high electrical conductivity is required. Furthermore, the oxygen content is higher according to EDX (6.3 at.%) compared to XPS (1.5 at.%). Again, this suggests that oxygen is not concentrated at the surface, as would be expected for hydrophilic surface functional groups or adsorbed water. As such, the oxygen content should not significantly affect the hydrophobicity of the material.

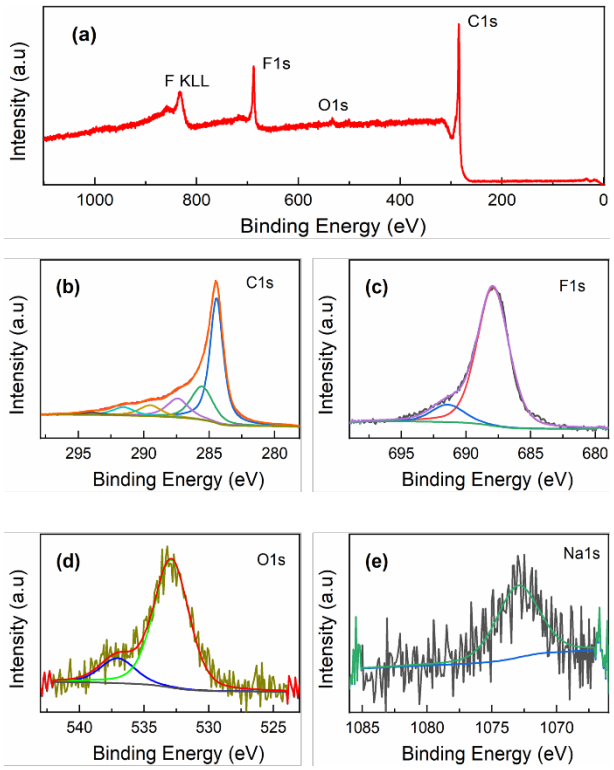

Figure 3: XPS of the fluorinated carbon sample: (a) survey spectrum; (b) C 1s; (c) F 1s; (d) O 1s; and (e) Na 1s regions.

Fig.4 shows thermogravimetric analysis (TGA) of the fluorinated carbon sample and graphitized carbon black, measured under constant air flow. The results show that the fluorinated carbon is thermally stable in air up until 500 °C, above which the material decomposes. Graphitized carbon black has slightly higher thermal stability, attributed to the lower thermodynamic stability of covalent C-F bonds compared to the C=C bonds in graphitized carbon black [31]. This confirms that this fluorinated carbon is resilient to thermal decomposition at typical temperatures used in PEFCs.

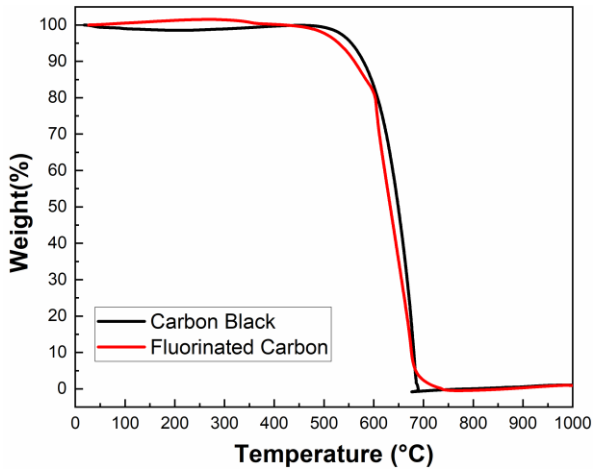

Figure 4: TGA of fluorinated carbon and graphitized carbon black in air.

3.2 Microporous Layer Characterization

The different microstructures of MPLs fabricated using fluorinated carbon (FC-MPL) and graphitized carbon black (CB-MPL) were investigated by SEM (Fig.5). In both cases, pores of several microns in size are observed, which is attributed to decomposition of the methyl cellulose pore forming agent, as expected. Meanwhile, the surface of the CB-MPL appears to be relatively smooth and uniform compared to that of the FC-MPL. This is attributed to the smaller particle diameter.

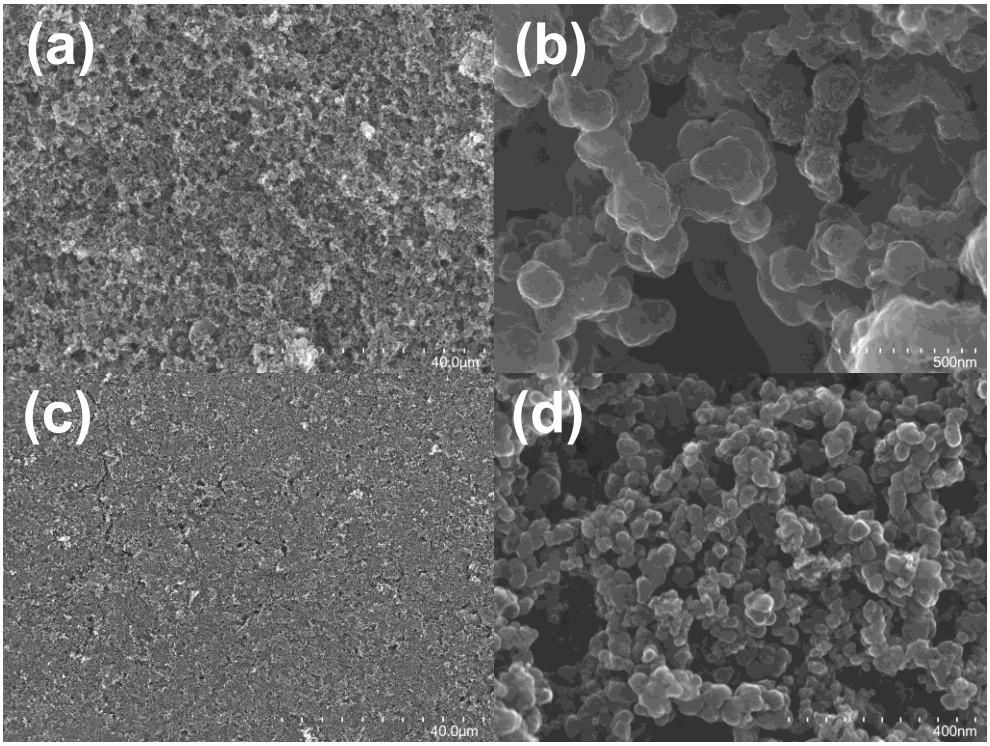

Figure 5: SEM images of MPL surface at different magnifications: (a-b) FC-MPL; (c-d) CB-MPL.

To confirm if fluorination of carbon can affect the water repelling properties of the resulting MPLs, the water contact angle (WCA) was measured and compared with other MPL-coated GDLs (Fig.6). The WCA of the as-synthesized fluorinated carbon sample (FC) after pressing is 160°, confirming that the synthesized material is indeed superhydrophobic (i.e. $\theta > 150°$). After incorporating the fluorinated carbon into an MPL (FC-MPL), the WCA is 151° (Fig. 6 (b)). This slight decrease is attributed to the effect of residual pore forming agent (methyl cellulose) added during slurry preparation, which does not completely decompose during the heating step (see TGA, Fig S3). Meanwhile, the WCA of the identically prepared CB-MPL is much lower at 131° (Fig. 6 (c)). Finally, the WCA of a commercial Toray-GDL (TGP-H-060, Toray, Japan) was measured to be 130° (Fig. 6 (d)). These results confirm that the

high WCA of the fluorinated carbon translates to significantly improved WCA in MPLs incorporating this material. The results also suggest that the WCA of the MPL is not dominated by the presence of the PTFE binder when the PTFE loading is sufficiently low (e.g. 5 wt%), but mainly instead on the properties of the carbon itself. This may not be the case for higher PTFE loading.

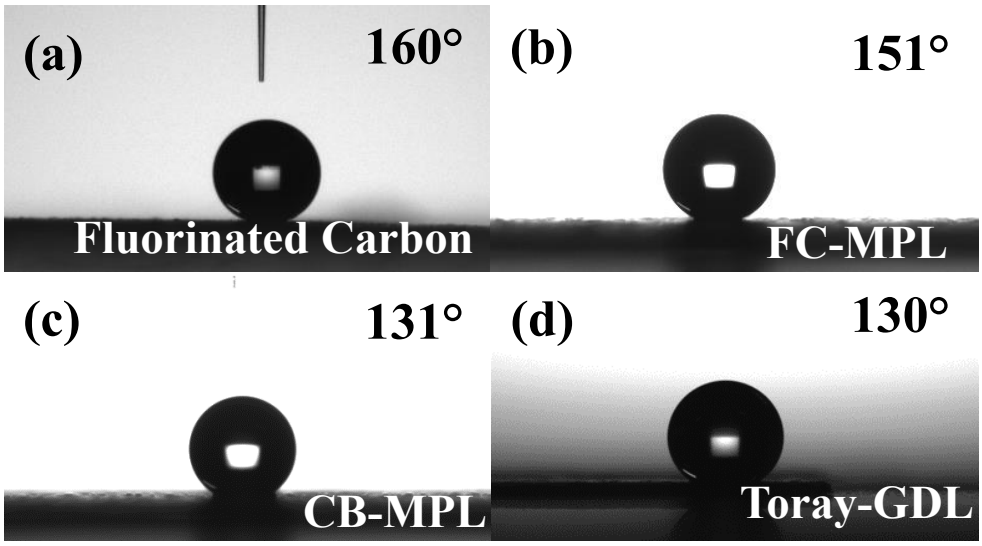

Figure 6. Surface water contact angle (WCA) measurements for: (a) pressed fluorinated carbon (FC); (b) FC-MPL; (c) CB-MPL; and (d) Toray-GDL (TGP-H-060).

Porosity is an important factor which affects mass transport resistance significantly. When porosity is increased, the total resistance to molecular diffusion in the system decreases. Here, the porosities of the free-standing FC-MPL and CB-MPL samples were calculated according to Eq.1 to be 76% and 83%, respectively, and the maximum pore diameters were similar at 42.5 and 40.5 μm (Fig.7(a)). Meanwhile, Toray-GDL had a larger maximum diameter of 61.7 μm, primarily because it does not include an MPL, exposing the larger pores defined by the spaces between carbon fibers.

The experimentally determined WCA above can be described as the *apparent contact angle*, which is dependent on both the surface interaction energy and the surface roughness of the sample. Once the maximum pore size has been determined, *Young's contact angle* can be estimated using the Young-Laplace Equation (Eq.3), and this value is independent of the surface roughness. Especially in this composite material, the Young's contact angle is an important parameter to confirm to what extent the apparent contact angle is due to the hydrophobic nature of the fluorinated carbon and what extent to the surface roughness. Both the Toray-GDL and the CB-MPL have similar Young's WCA of around 130° (Fig. 7(b)), consistent with the surface WCA measurement, and in agreement with prior studies [13]. In contrast, the Young's WCA for the FC-MPL is much higher at 151°. This agrees with the apparent WCA, confirming that the superhydrophobic nature of these MPLs is due to the nature of the material, rather than any change in surface roughness.

The through-plane air permeability was also measured (Fig.7(c)). FC-MPL has the lowest permeability, and CB-MPL has slightly higher permeability. Since the maximum pore diameter and the thickness of the CB-MPL and the FC-MPL are similar, the lower air permeability in FC-MPL may be the result of higher tortuosity due to lower porosity, and/or the smaller mean pore diameter. In contrast, the air permeability of Toray-GDL is over an order of magnitude higher, due to the much larger pores in the absence of an MPL. These results show that the air permeability is dominated by the MPL rather than the GDL.

Meanwhile, the oxygen transport resistance through the MPL-coated GDLs was measured in situ in a PEFC single cell (Fig.7(d)), as summarized in the experimental section. The results clearly show that the FC-MPL has significantly lower oxygen transport resistance compared to CB-MPL. For example, the oxygen transport resistance for the CB-MPL was measured to be 125 s/m at 80 ºC and 100 s/m at 45

ºC, compared to 105 s/m and 85 s/m for the FC-MPL under the same conditions. This is attributed to the superior water-repellent characteristics of FC-MPL, resulting in a faster rate of water removal. In all cases, the total oxygen transport resistance does not significantly vary with relative humidity, indicating that water accumulation in the MPL-coated GDLs and the catalyst layers does not change significantly under high humidity conditions [59,67].

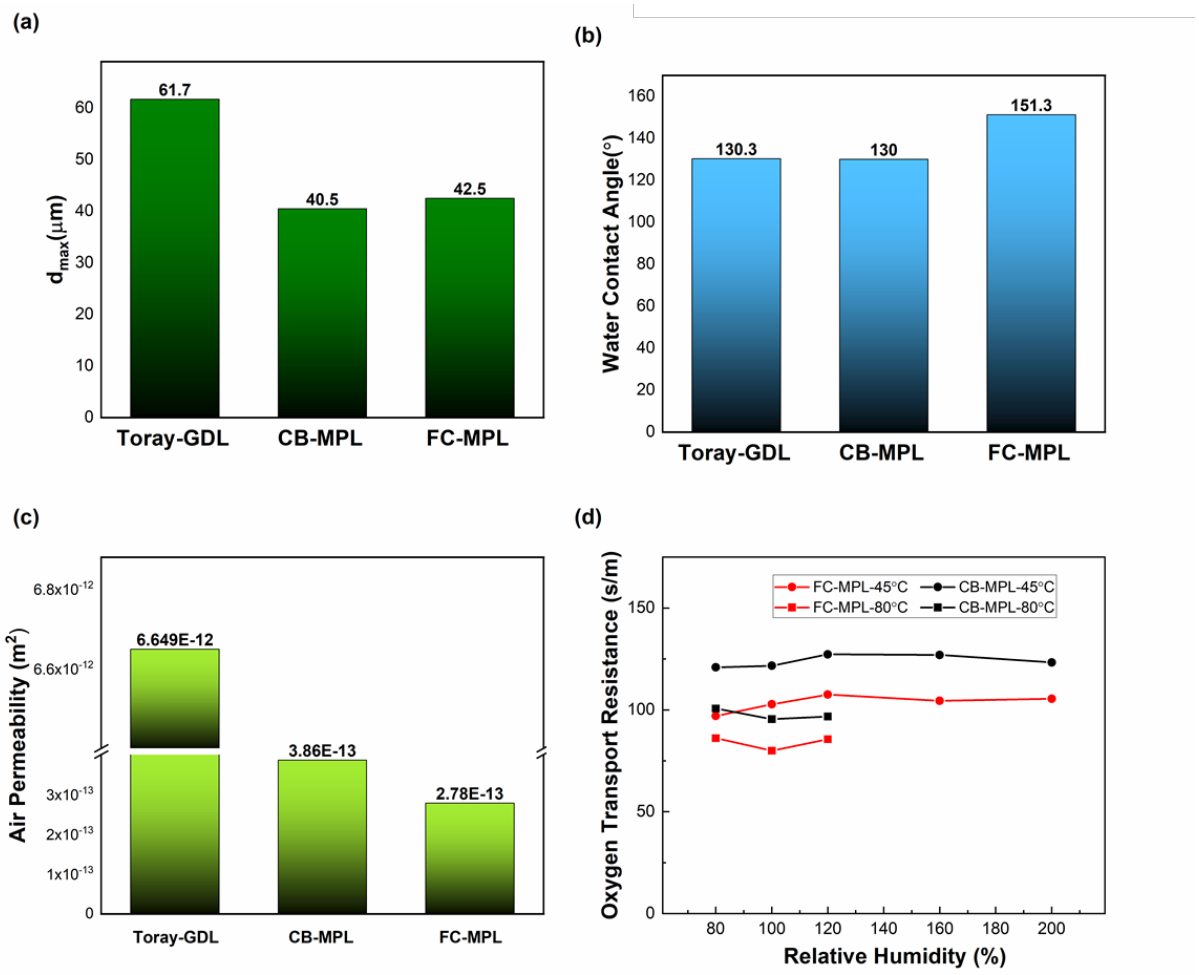

Figure 7: (a) Maximum pore diameter; (b) internal water contact angle; (c) air permeability; and (d) oxygen transport resistance for Toray-GDL, CB-MPL and FC-MPL.

3.3 Single Cell Characterization

Finally, PEFCs were fabricated incorporating the FC-MPL, and compared to identically prepared cells using the CB-MPL, at cell temperatures of 45 °C and 80 °C. At 45 °C, the performance of the cell was measured at 80, 100 and 120 % RH, whilst at 80 °C the cell was measured at 80 and 100 % RH.

The IR-free polarization curves reveal a clear difference in the mass diffusion limited current density region between the two MPLs, regardless of measurement temperature, with the FC-MPL cell having significantly higher cell voltage compared to the CB-MPL (Fig. 8 (a-b)). For example, at 80 °C and 80% RH, the limiting current densities were measured to be 1.61 A/cm^2 and 1.72 A/cm^2 for the CB-MPL and the FC-MPL, respectively. Similarly, at 45 °C and 80% the limiting current densities were measured to be ~1.03 A/cm^2 and 1.14 A/cm^2, respectively. This high current density region is where flooding normally occurs and disrupts oxygen diffusion to the catalyst surface, resulting in the observed voltage drop. However, the use of superhydrophobic fluorinated carbon in the MPL appears to improve removal of water from the cathode side of the cell, suppressing this voltage drop. This is confirmed and highlighted when the concentration overvoltage is separated from the polarization curves (Fig. 8(c-d).

Furthermore, when the ohmic regions of the polarization curves are compared, there is little difference between FC-MPL and CB-MPL (Fig. 8(e-f)). This indicates that the doping of electronegative fluorine atoms into the carbon structure does not significantly lower the electronic conductivity of the material, and therefore that ohmic losses can be avoided. As discussed in the elemental analysis section, this may be because the fluorine atoms are mainly concentrated at the surface of the carbon nanoparticles rather than throughout the bulk.

The effect of humidity on the polarization curves was also investigated. At the relatively low temperature of 45 ºC, the limiting current density does not change significantly with increasing humidity for either MPL-coated GDL. This may be because the amount of water which condenses at the cathode side of the cell does not change significantly between 80 and 120 % RH (as also inferred from oxygen transport resistance test results in Fig.7 (d)). Meanwhile, at higher cell temperature (80 ºC), there is a clear decrease in cell voltage as the relative humidity increase, especially in the mass diffusion limited current density region. This is attributed to a greater degree of water condensation at the cathode side of the cell at higher humidity, resulting in flooding and a corresponding voltage drop due to restriction of oxygen supply to the catalyst.

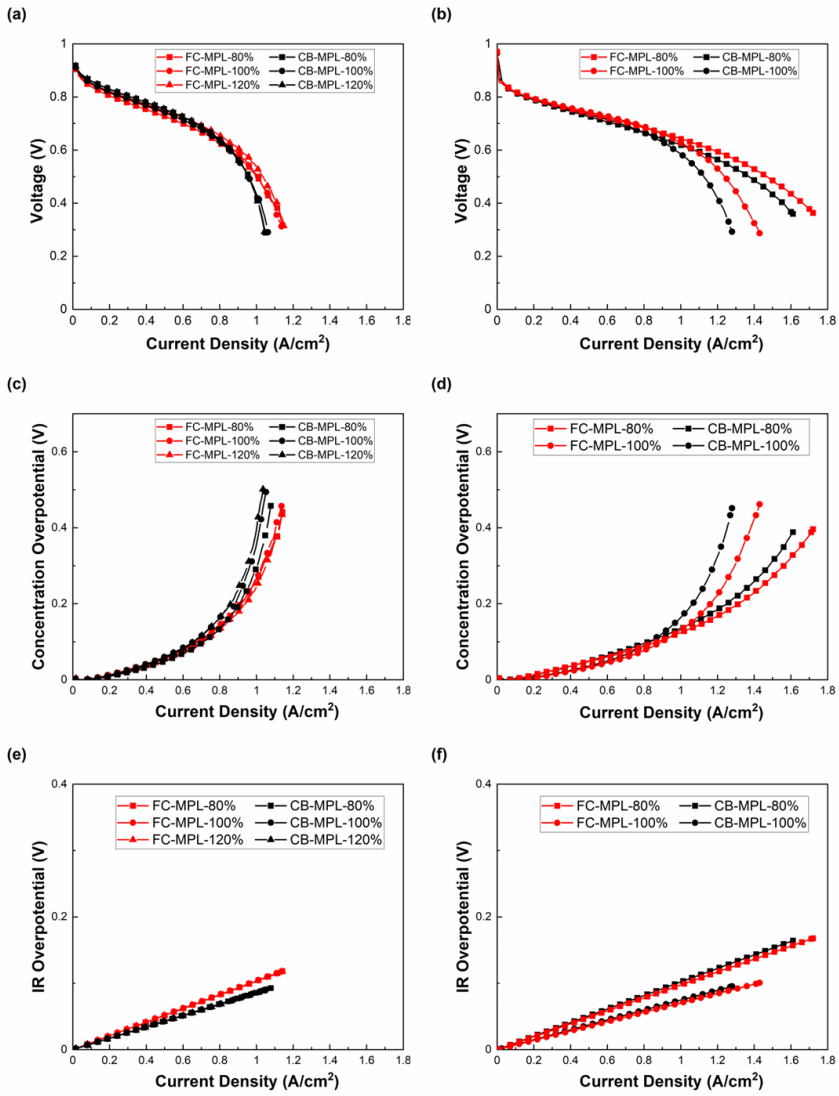

Figure 8: Single cell PEFC measurements under different relative humidity conditions. Polarization curves (IR-free) at cell temperatures of (a) 45 °C and (b) 80 °C. Concentration overvoltage at (c) 45 °C (d) 80 °C. IR overpotential at (e) 45 °C and (f) 80 °C.

CONCLUSIONS

In this paper, superhydrophobic fluorinated carbon nanoparticles were uniquely synthesized from fluorinated alcohol. The resulting superhydrophobic fluorinated carbon powder had similar microstructure and morphology to commercially

available carbon black, but with a fluorine content of 1.9 at.%. This powder was applied to a GDL to create a superhydrophobic MPL with a water contact angle of 151 º, despite the relatively low PTFE loading of 5 wt%. The FC-MPL displayed reproducibly superior I-V performance in a fuel cell at high current density. For example, at 80 °C and 80% RH the limiting current density was 1.61 A/cm^2 for the carbon black-based MPL, increasing to 1.72 A/cm^2 for the FC-MPL. These improvements in performance are attributed to lower oxygen transport resistance in the case of the FC-MPL (105 s/m at 80ºC) compared to CB-MPL (125 s/m at 80ºC). Therefore, the improved I-V performance is directly attributed to enhanced water removal from the microporous layer due to the superhydrophobic nature of the fluorinated carbon. This work is expected to result in the design of more efficient PEFCs which can operate at higher current density, with lower PTFE content.

ACKNOWLEDGEMENTS

Part of this study was supported by NEDO (Contract No. JPNP20003). Enes Muhammet Can acknowledges the Ph.D. scholarship funding provided by the Ministry of Education of Turkiye.

REFERENCES

[1] T. Abbasi, S.A. Abbasi, Is the use of renewable energy sources an answer to the problems of global warming and pollution?, Crit. Rev. Environ. Sci. Technol. 42 (2012) 99–154. https://doi.org/10.1080/10643389.2010.498754.

[2] S. Bilgen, S. Keleş, A. Kaygusuz, A. Sari, K. Kaygusuz, Global warming and renewable energy sources for sustainable development: A case study in

Turkey, Renew. Sustain. Energy Rev. 12 (2008) 372–396. https://doi.org/10.1016/j.rser.2006.07.016.

[3] I. Yüksel, Global warming and renewable energy sources for sustainable development in Turkey, Renew. Energy. 33 (2008) 802–812. https://doi.org/10.1016/j.renene.2007.05.040.

[4] K. Sasaki, H.-W. Li, A. Hayashi, J. Yamabe, T. Ogura, Hydrogen Energy Engineering, 2016. https://doi.org/10.1007/978-4-431-56042-5.

[5] J.O. Park, K. Kwon, M.D. Cho, S.-G. Hong, T.Y. Kim, D.Y. Yoo, Role of Binders in High Temperature PEMFC Electrode, J. Electrochem. Soc. 158 (2011) B675. https://doi.org/10.1149/1.3573773.

[6] S.M. Lyth, Doped and Decorated Carbon Foams for Energy Applications, Springer International Publishing, 2019. https://doi.org/10.1007/978-3-319-92917-0_8.

[7] A. Mufundirwa, G.F. Harrington, B. Smid, B. V. Cunning, K. Sasaki, S.M. Lyth, Durability of template-free Fe-N-C foams for electrochemical oxygen reduction in alkaline solution, J. Power Sources. 375 (2018) 244–254. https://doi.org/10.1016/j.jpowsour.2017.07.025.

[8] M. Breitwieser, T. Bayer, A. Büchler, R. Zengerle, S.M. Lyth, S. Thiele, A fully spray-coated fuel cell membrane electrode assembly using Aquivion ionomer with a graphene oxide/cerium oxide interlayer, J. Power Sources. 351 (2017) 145–150. https://doi.org/10.1016/j.jpowsour.2017.03.085.

[9] P.T. Moseley, Fuel Cell Systems Explained, 2001. https://doi.org/10.1016/s0378-7753(00)00571-1.

[10] H. Li, Y. Tang, Z. Wang, Z. Shi, S. Wu, D. Song, J. Zhang, K. Fatih, J.

Zhang, H. Wang, Z. Liu, R. Abouatallah, A. Mazza, A review of water flooding issues in the proton exchange membrane fuel cell, J. Power Sources. 178 (2008) 103–117. https://doi.org/10.1016/j.jpowsour.2007.12.068.

[11] U. Pasaogullari, C.Y. Wang, Two-phase transport and the role of micro-porous layer in polymer electrolyte fuel cells, Electrochim. Acta. 49 (2004) 4359–4369. https://doi.org/10.1016/j.electacta.2004.04.027.

[12] M.S. Ismail, T. Damjanovic, D.B. Ingham, M. Pourkashanian, A. Westwood, Effect of polytetrafluoroethylene-treatment and microporous layer-coating on the electrical conductivity of gas diffusion layers used in proton exchange membrane fuel cells, J. Power Sources. 195 (2010) 2700–2708. https://doi.org/10.1016/j.jpowsour.2009.11.069.

[13] T. Van Nguyen, A. Ahosseini, X. Wang, V. Yarlagadda, A. Kwong, A.Z. Weber, P. Deevanhxay, S. Tsushima, S. Hirai, Hydrophobic Gas-Diffusion Media for Polymer-Electrolyte Fuel Cells by Direct Fluorination, J. Electrochem. Soc. 162 (2015) F1451–F1460. https://doi.org/10.1149/2.0411514jes.

[14] J. Zhang, B. Wang, J. Jin, S. Yang, G. Li, A review of the microporous layer in proton exchange membrane fuel cells: Materials and structural designs based on water transport mechanism, Renew. Sustain. Energy Rev. 156 (2022) 111998. https://doi.org/10.1016/j.rser.2021.111998.

[15] R. Lin, X. Yu, L. Chen, S. Tang, X. Yin, Z. Hao, Structure majorization on the surface of microporous layer in polymer electrolyte membrane fuel cells to optimize performance and durability, Energy Convers. Manag. 243 (2021) 114319. https://doi.org/10.1016/j.enconman.2021.114319.

[16] L. Chen, R. Lin, S. Tang, D. Zhong, Z. Hao, Structural design of gas

diffusion layer for proton exchange membrane fuel cell at varying humidification, J. Power Sources. 467 (2020) 228355. https://doi.org/10.1016/j.jpowsour.2020.228355.

[17] Y. Tabe, Y. Aoyama, K. Kadowaki, K. Suzuki, T. Chikahisa, Impact of micro-porous layer on liquid water distribution at the catalyst layer interface and cell performance in a polymer electrolyte membrane fuel cell, J. Power Sources. 287 (2015) 422–430. https://doi.org/10.1016/j.jpowsour.2015.04.095.

[18] F. Aldakheel, M.S. Ismail, K.J. Hughes, D.B. Ingham, L. Ma, M. Pourkashanian, D. Cumming, R. Smith, Gas permeability, wettability and morphology of gas diffusion layers before and after performing a realistic ex-situ compression test, Renew. Energy. 151 (2020) 1082–1091. https://doi.org/10.1016/j.renene.2019.11.109.

[19] O.M. Orogbemi, D.B. Ingham, M.S. Ismail, K.J. Hughes, L. Ma, M. Pourkashanian, On the gas permeability of the microporous layer used in polymer electrolyte fuel cells, J. Energy Inst. 91 (2018) 894–901. https://doi.org/10.1016/j.joei.2017.09.006.

[20] M.S. Ismail, D. Borman, T. Damjanovic, D.B. Ingham, M. Pourkashanian, On the through-plane permeability of microporous layer-coated gas diffusion layers used in proton exchange membrane fuel cells, Int. J. Hydrogen Energy. 36 (2011) 10392–10402. https://doi.org/10.1016/j.ijhydene.2010.09.012.

[21] O.M. Orogbemi, D.B. Ingham, M.S. Ismail, K.J. Hughes, L. Ma, M. Pourkashanian, The effects of the composition of microporous layers on the permeability of gas diffusion layers used in polymer electrolyte fuel cells, Int. J. Hydrogen Energy. 41 (2016) 21345–21351.

https://doi.org/10.1016/j.ijhydene.2016.09.160.

[22] C. Simon, D. Kartouzian, D. Müller, F. Wilhelm, H.A. Gasteiger, Impact of Microporous Layer Pore Properties on Liquid Water Transport in PEM Fuel Cells: Carbon Black Type and Perforation, J. Electrochem. Soc. 164 (2017) F1697–F1711. https://doi.org/10.1149/2.1321714jes.

[23] C.M. Long, M.A. Nascarella, P.A. Valberg, Carbon black vs. black carbon and other airborne materials containing elemental carbon: Physical and chemical distinctions, Environ. Pollut. 181 (2013) 271–286. https://doi.org/10.1016/j.envpol.2013.06.009.

[24] J.T. Gostick, M.A. Ioannidis, M.W. Fowler, M.D. Pritzker, On the role of the microporous layer in PEMFC operation, Electrochem. Commun. 11 (2009) 576–579. https://doi.org/10.1016/j.elecom.2008.12.053.

[25] C. Li, D. Si, Y. Liu, J. Zhang, Y. Liu, Water management characteristics of electrospun micro-porous layer in PEMFC under normal temperature and cold start conditions, Int. J. Hydrogen Energy. 46 (2021) 11150–11159. https://doi.org/10.1016/j.ijhydene.2020.05.271.

[26] C.J. Tseng, S.K. Lo, Effects of microstructure characteristics of gas diffusion layer and microporous layer on the performance of PEMFC, Energy Convers. Manag. 51 (2010) 677–684. https://doi.org/10.1016/j.enconman.2009.11.011.

[27] A.T. Najafabadi, M.J. Leeuwner, D.P. Wilkinson, E.L. Gyenge, Electrochemically Produced Graphene for Microporous Layers in Fuel Cells, ChemSusChem. 9 (2016) 1689–1697. https://doi.org/10.1002/cssc.201600351.

[28] G. Lin, T. Van Nguyen, Effect of Thickness and Hydrophobic Polymer

Content of the Gas Diffusion Layer on Electrode Flooding Level in a PEMFC, J. Electrochem. Soc. 152 (2005) A1942. https://doi.org/10.1149/1.2006487.

[29] M.S. Ismail, K.J. Hughes, D.B. Ingham, L. Ma, M. Pourkashanian, Effect of PTFE loading of gas diffusion layers on the performance of proton exchange membrane fuel cells running at high-efficiency operating conditions, Int. J. Energy Res. 37 (2013) 1592–1599. https://doi.org/10.1002/er.2968.

[30] S.M. Lyth, W. Ma, J. Liu, T. Daio, K. Sasaki, A. Takahara, B. Ameduri, Solvothermal synthesis of superhydrophobic hollow carbon nanoparticles from a fluorinated alcohol, Nanoscale. 7 (2015) 16087–16093. https://doi.org/10.1039/c5nr03484a.

[31] O. V. Boltalina, T. Nakajima, New Fluorinated Carbons: Fundamentals and Applications Progress in Fluorine Science Series, 2016. https://doi.org/10.1016/C2014-0-04885-X.

[32] C. Te Hsieh, W.Y. Chen, F.L. Wu, Fabrication and superhydrophobicity of fluorinated carbon fabrics with micro/nanoscaled two-tier roughness, Carbon N. Y. 46 (2008) 1218–1224. https://doi.org/10.1016/j.carbon.2008.04.026.

[33] E.T. Mickelson, C.B. Huffman, A.G. Rinzler, R.E. Smalley, R.H. Hauge, J.L. Margrave, Fluorination of single-wall carbon nanotubes, Chem. Phys. Lett. 296 (1998) 188–194. https://doi.org/10.1016/S0009-2614(98)01026-4.

[34] N.O.V. Plank, L. Jiang, R. Cheung, Fluorination of carbon nanotubes in CF4 plasma, Appl. Phys. Lett. 83 (2003) 2426–2428. https://doi.org/10.1063/1.1611621.

[35] M. Adamska, U. Narkiewicz, Fluorination of Carbon Nanotubes − A Review,

J. Fluor. Chem. 200 (2017) 179–189. https://doi.org/10.1016/j.jfluchem.2017.06.018.

[36] Y.S. Lee, Synthesis and characterization of fluorinated carbon fibers and nanotubes, Elsevier Inc., 2017. https://doi.org/10.1016/B978-0-12-803479-8.00006-1.

[37] S.J. Park, M.K. Seo, Y.S. Lee, Surface characteristics of fluorine-modified PAN-based carbon fibers, Carbon N. Y. 41 (2003) 723–730. https://doi.org/10.1016/S0008-6223(02)00384-6.

[38] F. Chamssedine, M. Dubois, K. Guérin, J. Giraudet, F. Masin, D.A. Ivanov, L. Vidal, R. Yazami, A. Hamwi, Reactivity of carbon nanofibers with fluorine gas, Chem. Mater. 19 (2007) 161–172. https://doi.org/10.1021/cm061731m.

[39] W. Kang, S. Li, Preparation of fluorinated graphene to study its gas sensitivity, RSC Adv. 8 (2018) 23459–23467. https://doi.org/10.1039/C8RA03451F.

[40] B. Shen, J. Chen, X. Yan, Q. Xue, Synthesis of fluorine-doped multi-layered graphene sheets by arc-discharge, RSC Adv. 2 (2012) 6761–6764. https://doi.org/10.1039/c2ra20593a.

[41] A. Hamwi, M. Daoud, J.C. Cousseins, Graphite fluorides prepared at room temperature 1. Synthesis and characterization, Synth. Met. 26 (1988) 89–98. https://doi.org/10.1016/0379-6779(88)90338-4.

[42] B. Wang, J. Wang, J. Zhu, Fluorination of graphene: A Spectroscopic and microscopic study, ACS Nano. 8 (2014) 1862–1870. https://doi.org/10.1021/nn406333f.

[43] G. Nansé, E. Papirer, P. Fioux, F. Moguet, A. Tressaud, Fluorination of carbon blacks: An X-ray photoelectron spectroscopy study: I. A literature review of XPS studies of fluorinated carbons. XPS investigation of some reference compounds, Carbon N. Y. 35 (1997) 175–194. https://doi.org/10.1016/S0008-6223(96)00095-4.

[44] N. Watanabe, Y. Kita, O. Mochizuki, Fluorination of carbon black, Carbon N. Y. 17 (1979) 359–363. https://doi.org/10.1016/0008-6223(79)90009-5.

[45] K. Guérin, M. Dubois, A. Houdayer, A. Hamwi, Applicative performances of fluorinated carbons through fluorination routes: A review, J. Fluor. Chem. 134 (2012) 11–17. https://doi.org/10.1016/j.jfluchem.2011.06.013.

[46] C.A.S. Hall, K.A. Klitgaard, Energy and the wealth of nations: Understanding the biophysical economy, 2012. https://doi.org/10.1007/978-1-4419-9398-4.

[47] J.S. Im, S.C. Kang, S.H. Lee, Y.S. Lee, Improved gas sensing of electrospun carbon fibers based on pore structure, conductivity and surface modification, Carbon N. Y. 48 (2010) 2573–2581. https://doi.org/10.1016/j.carbon.2010.03.045.

[48] Z. Fang, Y. Peng, X. Zhou, L. Zhu, Y. Wang, X. Dong, Y. Xia, Fluorinated Carbon Materials and the Applications in Energy Storage Systems, ACS Appl. Energy Mater. (2021). https://doi.org/10.1021/acsaem.1c03476.

[49] Q. Zhang, K.J. Takeuchi, E.S. Takeuchi, A.C. Marschilok, Progress towards high-power Li/CFx batteries: Electrode architectures using carbon nanotubes with CFx, Phys. Chem. Chem. Phys. 17 (2015) 22504–22518. https://doi.org/10.1039/c5cp03217b.

[50] F.A. Viva, G.A. Olah, G.K.S. Prakash, Characterization of Pt supported on commercial fluorinated carbon as cathode catalysts for Polymer Electrolyte Membrane Fuel Cell, Int. J. Hydrogen Energy. 42 (2017) 15054–15063. https://doi.org/10.1016/j.ijhydene.2017.04.255.

[51] J.L. Bott-Neto, T. Asset, F. Maillard, L. Dubau, Y. Ahmad, K. Guérin, S. Berthon-Fabry, A. Mosdale, R. Mosdale, E.A. Ticianelli, M. Chatenet, Utilization of graphitized and fluorinated carbon as platinum nanoparticles supports for application in proton exchange membrane fuel cell cathodes, J. Power Sources. 404 (2018) 28–38. https://doi.org/10.1016/j.jpowsour.2018.10.004.

[52] S. Berthon-Fabry, L. Dubau, Y. Ahmad, K. Guerin, M. Chatenet, First Insight into Fluorinated Pt/Carbon Aerogels as More Corrosion-Resistant Electrocatalysts for Proton Exchange Membrane Fuel Cell Cathodes, Electrocatalysis. 6 (2015) 521–533. https://doi.org/10.1007/s12678-015-0267-9.

[53] Carbon black CP 1333-86-4. https://www.sigmaaldrich.com/JP/en/product/saj/051530. (accessed July 28, 2022).

[54] Polytetrafluoroethylene (Teflon^{TM} 30B) 60 wt % Dispersion. https://www.polysciences.com/india/poly-teflon-30b (accessed July 28, 2022).

[55] C. Simon, D. Kartouzian, D. Müller, F. Wilhelm, H.A. Gasteiger, Impact of Microporous Layer Pore Properties on Liquid Water Transport in PEM Fuel Cells: Carbon Black Type and Perforation, J. Electrochem. Soc. 164 (2017) F1697–F1711. https://doi.org/10.1149/2.1321714jes.

[56] C. Simon, J. Endres, B. Nefzger-Loders, F. Wilhelm, H.A. Gasteiger, Interaction of Pore Size and Hydrophobicity/Hydrophilicity for Improved Oxygen and Water Transport through Microporous Layers, J. Electrochem. Soc. 166 (2019) F1022–F1035. https://doi.org/10.1149/2.1111913jes.

[57] L. Cindrella, A.M. Kannan, J.F. Lin, K. Saminathan, Y. Ho, C.W. Lin, J. Wertz, Gas diffusion layer for proton exchange membrane fuel cells-A review, J. Power Sources. 194 (2009) 146–160. https://doi.org/10.1016/j.jpowsour.2009.04.005.

[58] M. Okumura, Z. Noda, J. Matsuda, Y. Tachikawa, M. Nishihara, S.M. Lyth, A. Hayashi, K. Sasaki, Correlating Cathode Microstructure with PEFC Performance Using FIB-SEM and TEM, J. Electrochem. Soc. 164 (2017) F928–F934. https://doi.org/10.1149/2.0581709jes.

[59] T. Kitahara, H. Nakajima, Microporous layer-coated gas diffusion layer to reduce oxygen transport resistance in a polymer electrolyte fuel cell under high humidity conditions, Int. J. Hydrogen Energy. 41 (2016) 9547–9555. https://doi.org/10.1016/j.ijhydene.2016.04.117.

[60] M.F. Mathias, J. Roth, J. Fleming, W. Lehnert, Diffusion media materials and characterisation, Handb. Fuel Cells. (2010). https://doi.org/10.1002/9780470974001.f303046.

[61] J.I.S.C.P. and board D. of air permeance-G. method J.P. 8117 (1998), GURLEY Method for air permeability.pdf, n.d.

[62] H. Yasuda, K. Kobayashi, A. Daimaru, M. Hori, Measurement of Oxygen Gas Transport Resistance in Cathode Catalyst Layers of PEFC, ECS Meet. Abstr. MA2014-01 (2014) 811–811. https://doi.org/10.1149/ma2014-01/18/811.

[63] M. Thommes, K. Kaneko, A. V. Neimark, J.P. Olivier, F. Rodriguez-Reinoso, J. Rouquerol, K.S.W. Sing, Physisorption of gases, with special reference to the evaluation of surface area and pore size distribution (IUPAC Technical Report), Pure Appl. Chem. 87 (2015) 1051–1069. https://doi.org/10.1515/pac-2014-1117.

[64] J.H. Chun, D.H. Jo, S.G. Kim, S.H. Park, C.H. Lee, S.H. Kim, Improvement of the mechanical durability of micro porous layer in a proton exchange membrane fuel cell by elimination of surface cracks, Renew. Energy. 48 (2012) 35–41. https://doi.org/10.1016/j.renene.2012.04.011.

[65] G. Thiele, M. Poston, R. Brown, A case study sizing Nanoparticles, 234th ACS Natl. Meet. (2007) 316.

[66] K.H. An, J.G. Heo, K.G. Jeon, D.J. Bae, C. Jo, C.W. Yang, C.Y. Park, Y.H. Lee, Y.S. Lee, Y.S. Chung, X-ray photoemission spectroscopy study of fluorinated single-walled carbon nanotubes, Appl. Phys. Lett. 80 (2002) 4235–4237. https://doi.org/10.1063/1.1482801.

[67] N. Nonoyama, S. Okazaki, A.Z. Weber, Y. Ikogi, T. Yoshida, Analysis of Oxygen-Transport Diffusion Resistance in Proton-Exchange-Membrane Fuel Cells, J. Electrochem. Soc. 158 (2011) B416. https://doi.org/10.1149/1.3546038.